Quantum-state tomography of single-photon entangled states

E. T. Burch, C. Henelsmith, W. Larson, and M. Beck*
Department of Physics, Whitman College, Walla Walla, Washington 99362, USA
(Received 4 August 2015; published 28 September 2015)

We have performed quantum-state tomography on several different single-photon entangled states, that is, states in which a single photon is shared between two possible paths. We begin by doing a tomographic reconstruction of density matrices in the subspace where a single photon is shared by two spatial modes. In this subspace we are able to create high-fidelity, path-entangled states. Also within this subspace we use the Akaike information criterion and Monte Carlo simulations to help us estimate the amount and source of state drift in our system. We find that the primary state drift is due to phase drifts and fluctuations on the order of $\pi/400$ in our experimental apparatus. We then use the single-photon subspace density matrices and further measurements to estimate density matrices in the larger space consisting of two modes containing up to one photon each. In this larger space we find that the concurrence of the density matrices is $C \cong 0.08$ and is greater than 0 by at least 45 standard deviations, indicating that our states are indeed entangled.

DOI: 10.1103/PhysRevA.92.032328 PACS number(s): 03.67.Bg, 03.67.Mn, 03.65.Ud, 03.65.Wj

I. INTRODUCTION

Consider a single photon incident on a beam splitter, as shown in the upper-left corner of Fig. 1. The photon can be reflected, or transmitted where it then undergoes a phase shift θ. The single photon is now shared between both output modes, and its state can be written as

$$|\psi\rangle = a|1\rangle_r|0\rangle_t + be^{i\theta}|0\rangle_r|1\rangle_t = a|1,0\rangle + be^{i\theta}|0,1\rangle. \quad (1)$$

Here a and b are real numbers determined by the beam splitter reflectivity and that satisfy the normalization condition $a^2 + b^2 = 1$. Equation (1) represents a mode-entangled state of a single photon [1,2], and states of this form have potential applications in quantum networking [3]. These states are also known as single-photon entangled states.

There are several ways to perform state measurements on, or to witness entanglement in, single-photon entangled states. One way is to perform homodyne detection on each of the output modes from the beam splitter and use these measurements to tomographically determine the full joint quantum state [4]. Other techniques determine an entanglement witness rather than the full quantum state [5,6]. Violations of Bell-type inequalities have been reported for single-photon entangled states [4,7], as has a violation of an Einstein-Podolsky-Rosen steering inequality [8]. All of these techniques require a local oscillator that is mode matched to the state being measured.

Several experiments have been performed in which states having the form of Eq. (1) have been stored in atomic ensembles or crystals, and then read out and characterized [9–12]. In each of these experiments entanglement was demonstrated by measuring the concurrence of the density matrix. The diagonal elements of the density matrix were measured by photon counting, while the magnitudes of the off-diagonal elements were determined by measuring both photocounts and the visibility of a fringe pattern measured at many different relative phases.

Finally, we note that single-photon entangled states have been successfully purified [13]. Purification of these states will likely be necessary for them to be useful in practical quantum networking applications operating over long distances.

Here we use a two-step process to measure our states, and to demonstrate that they are entangled. We do not use a local oscillator, but instead characterize the states using photon counting, so our technique is more similar to those of Refs. [9–12]. First we limit ourselves to the subspace of a single photon. Within this subspace we measure the density matrix of the path-entangled states using maximum-likelihood quantum-state tomography [14]. This technique yields the full complex density matrix, not just the magnitude of the density matrix as was obtained in previous experiments using photon counting. Also, since this measurement technique is based on the standard tomographic technique of performing measurements in different bases, it will be extendable to measurements of single photons entangled in other degrees of freedom beyond just their path after a beam splitter (e.g., in polarization as well).

Furthermore, to characterize time-dependent drifts of the state, we perform two separate sets of tomographic measurements in succession. We use five projections for each successive state determination, and we determine three different states. The first is the state of the first five projections, the second is the state of the second five projections, and the third is the state determined by all ten projections. We then apply the Akaike information criterion (AIC) as described in Ref. [15]. By comparing the AIC and other measures of the states to Monte Carlo simulations of the experiments, we are able to estimate the size of the state drift in our system. The AIC has been used previously to characterize different aspects of quantum systems [16,17]; here it is used to characterize the drift of a quantum state.

Once the measurements that determine the state in the single-photon subspace are complete, we perform further measurements to determine the density matrix in the expanded space containing up to one photon in each mode [9–12]. The degree of entanglement is characterized by the concurrence C of this density matrix, and $C > 0$ ensures that our state is entangled within this larger space [9,18]. Finally, as a

*beckmk@whitman.edu

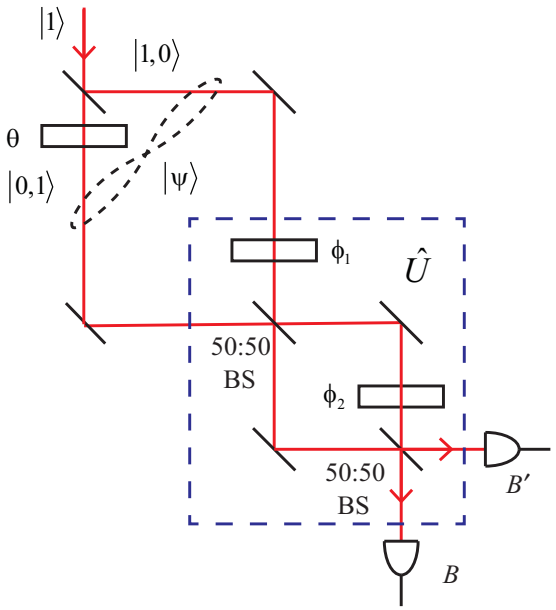

FIG. 1. (Color online) A single photon is incident on a beam splitter, and the path-entangled state $|\psi\rangle$ is created at the output modes of the beam splitter. An interferometer (dashed box) implements the transformation $\hat{U}(\phi_1,\phi_2)$ and the outputs are detected.

further measure of the suppression of two-photon events in our heralded one-photon source, we measure the degree of second-order coherence $g^{(2)}(0)$ [19–22] and show that this measurement is consistent with that of a single photon.

II. THEORY

A. Quantum-state tomography

Consider the configuration shown in Fig. 1. A single photon is incident on a beam splitter, and the state $|\psi\rangle$ of Eq. (1) is created at the beam splitter outputs (for the moment we assume that we are working in the subspace of a single photon). The two modes of this state are fed into the input ports of an interferometer that is constructed of 50:50 beam splitters and has two adjustable phases ϕ_1 and ϕ_2. The unitary operator for this interferometer, which transforms the input modes into the modes at the two detectors, can be represented as

$$\hat{U}(\phi_1,\phi_2) = \frac{1}{2}\begin{pmatrix} -e^{i\phi_1}(1+e^{i\phi_2}) & (-1+e^{i\phi_2}) \\ e^{i\phi_1}(1-e^{i\phi_2}) & (1+e^{i\phi_2}) \end{pmatrix}. \quad (2)$$

Essentially, this interferometer behaves as a beam splitter whose reflection and transmission coefficients can be adjusted using ϕ_1 and ϕ_2; this is what makes it useful for our purposes here.

To perform quantum-state tomography, it is necessary to make measurements in bases corresponding to different linear combinations of the input states. For appropriate choices of the phases, the transformations described by $\hat{U}(\phi_1,\phi_2)$ allow one to do this. For example, when applying the transformation $\hat{U}(0,0)$ the input states $|1,0\rangle$ and $|0,1\rangle$ are unchanged (apart from inconsequential overall phase shifts), and are measured directly by the detectors. The transformation $\hat{U}(\pi/2,\pi/2)$ maps the states

$$|\psi_1\rangle = \frac{1}{\sqrt{2}}(|1,0\rangle + |0,1\rangle), \quad (3)$$

$$|\psi_2\rangle = \frac{1}{\sqrt{2}}(|1,0\rangle - |0,1\rangle) \quad (4)$$

onto the detectors, while $\hat{U}(0,\pi/2)$ maps the states

$$|\psi_3\rangle = \frac{1}{\sqrt{2}}(|1,0\rangle + i|0,1\rangle), \quad (5)$$

$$|\psi_4\rangle = \frac{1}{\sqrt{2}}(|1,0\rangle - i|0,1\rangle) \quad (6)$$

onto the detectors.

In the basis $|0,1\rangle$, $|1,0\rangle$, the single-photon entangled state of Eq. (1) has as its density matrix representation

$$\hat{\rho}^{(1)} = \begin{pmatrix} b^2 & abe^{-i\theta} \\ abe^{i\theta} & a^2 \end{pmatrix}. \quad (7)$$

In general, within the subspace of a single photon, the density matrix is given by

$$\hat{\rho}^{(1)} = \begin{pmatrix} \beta & \gamma \\ \gamma^* & \alpha \end{pmatrix}. \quad (8)$$

Here γ is complex, while α and β are real and positive and satisfy the normalization condition $\alpha+\beta=1$. We use maximum-likelihood quantum-state tomography in order to determine density matrices of this form [14]. For our two-dimensional system this technique requires measurements to be performed in a minimum of three different bases. We perform measurements in five bases (i.e., five different settings of ϕ_1 and ϕ_2).

B. The Akaike information criterion

The AIC is a method to rank different models, in order to determine which best fits a set of measured data. As described by van Enk and Blume-Kohout in Ref. [15], the AIC assigns a number Ω_k to each model k, given by

$$\Omega_k = \ln \mathcal{L}_k - K_k. \quad (9)$$

Here $\mathcal{L}_k$ is the maximum likelihood of model k, and K_k is the number of independent parameters used in the model to fit the data. Roughly speaking, the difference $\Delta\Omega = \Omega_k - \Omega_{k'}$ is the weight of evidence (in bits) of model k over model k'. The basic idea behind the AIC is that models with larger likelihood are better, but there is a "penalty" for increasing the number of adjustable parameters in order to improve the model fit. This is a way of guarding against overfitting the data.

In our experiments, for measurement j we acquire data from N_j qubits, the result being that a photon is registered at either detector B or detector B'. We then change the settings of the measurement apparatus (the phases of the interferometer) and repeat this process, at a total of M measurement settings. For measurement j the logarithm of the likelihood is given by

$$\ln \mathcal{L}^{(j)} = N_j f_B^{(j)} \ln\left(p_B^{(j)}\right) + N_j f_{B'}^{(j)} \ln\left(p_{B'}^{(j)}\right), \quad (10)$$

where $f_B^{(j)}$ and $f_{B'}^{(j)}$ are the fractions of the measurements that yield B and B', respectively, and $p_B^{(j)}$ and $p_{B'}^{(j)}$ are the

probabilities of B and B' measurements determined from the density matrix returned by maximum-likelihood tomography. The total logarithm of the likelihood is obtained by summing over the M measurement settings:

$$\ln \mathcal{L} = \sum_{j=1}^{M} \ln \mathcal{L}^{(j)}. \tag{11}$$

We use five measurement settings and maximum-likelihood tomography to determine a density matrix for one of our experimentally produced states, and then repeat these five measurements to determine a second density matrix. We then use all ten measurements to determine the density matrix of the entire ensemble. We refer to this ten-measurement model as the standard model. Since it returns a single density matrix with three independent, real parameters [Eq. (8)], it has $K_s = 3$ and returns an AIC value of Ω_s. The alternative model uses the separate five-measurement subsets, and returns two independent density matrices, which have a total of six independent parameters. The alternative model thus has $K_a = 6$ and returns an AIC value of Ω_a. We then compute the difference $\Delta\Omega = \Omega_s - \Omega_a$.

To understand what we expect from the AIC difference, first consider the unphysical situation in which there are no fluctuations in the data, and hence all three density matrices that we determine are the same. In this case the likelihoods of the two models are the same, and the only difference between them is the number of independent parameters. Since the standard model uses three fewer parameters, it pays less of a penalty, and we have $\Delta\Omega = 3$. This positive value tells us that the standard model is "better" because it contains the same information, but uses fewer parameters.

If there is any drift in the state between measurements, the three density matrices will be different. Note that in this case the likelihood of the alternative model will be higher than that of the standard model, as two separate density matrices will be able to reflect this drift better than a single density matrix. Thus, the question the AIC difference $\Delta\Omega$ helps us to address is not which model is more likely, but whether or not the additional free parameters of the alternative model are justified. In an experiment we will always have $\Delta\Omega < 3$.

The value of $\Delta\Omega$ gives us an idea of how much drift there is in our states; larger values correspond to less drift. Even if $\Delta\Omega$ is negative, indicating that there is drift in the state, it may be that the amount of drift is within acceptable limits. To assess this, we compare our experimental measurements of $\Delta\Omega$ to Monte Carlo simulations of our data. These simulations include the primary sources of experimental imperfections in our experiments: Poissonian noise of the counting statistics, accidental coincidences due to our finite coincidence windows, and phase drift and fluctuations in the interferometer. The simulations help us to obtain an understanding of how these imperfections influence the state drift in our experiments.

C. Concurrence of $\hat{\rho}$ in the larger Hilbert space

Above we have assumed that our Hilbert space contains exactly one photon. However, our heralded photon source is not 100% efficient, so there is some probability that there are zero photons present. There is also a very small probability that there are two photons within the coincidence window of our detectors. We must allow for these possibilities when examining whether or not the states that we measure are truly entangled.

To do this, we construct the density matrix for our experimentally determined states within a larger Hilbert space that contains up to one photon in each output port of the first beam splitter of Fig. 1. Following Chou *et al.* we write this density matrix as [9]

$$\hat{\rho}^{(2)} = \begin{pmatrix} p_{00} & 0 & 0 & 0 \\ 0 & p_{01} & d & 0 \\ 0 & d^* & p_{10} & 0 \\ 0 & 0 & 0 & p_{11} \end{pmatrix}. \tag{12}$$

This matrix is written in the basis $|n\rangle_r|m\rangle_t$, with the number of photons in the reflected or transmitted modes being 0 or 1. The form of Eq. (12) assumes that the off-diagonal elements corresponding to different numbers of photons in the two modes are zero, and that terms with two or more photons per mode are also zero. It can be shown that these assumptions can only decrease the amount of measured entanglement, so they set a lower bound on the amount of entanglement actually present in the experiments [9].

To determine this density matrix, after the ten measurements that determine the state $\hat{\rho}^{(1)}$ in the subspace of a single photon, we set the phases of our interferometer (Fig. 1) to $\phi_1 = \phi_2 = 0$ and perform ten more measurements. (Ten measurements allow us to determine the standard deviation of our measurements, which we use to express all of our errors.) This setting directs the two modes after the first beam splitter (Fig. 1) directly onto the detectors B and B', so we can determine the probabilities of obtaining 0 or 1 photons in each beam. For our spontaneous parametric down-conversion source, in which the presence of a signal photon in our interferometer is heralded by the detection of an idler photon at detector A, the probability of detecting one photon in each interferometer beam is

$$p_{11} = \frac{N_{ABB'}}{N_A}. \tag{13}$$

Here we use the notation that within our measurement time N_j is the number of counts on detector j, N_{Aj} is the number of coincidences between detectors A and j, and $N_{ABB'}$ is the measured number of threefold coincidences. The probability of detecting a single photon (in either mode) is given by

$$\begin{aligned} P_1 &= \frac{(N_{AB} - N_{ABB'}) + (N_{AB'} - N_{ABB'})}{N_A} \\ &= \frac{N_{AB} + N_{AB'} - 2N_{ABB'}}{N_A}, \end{aligned} \tag{14}$$

and the probability of detecting zero photons is

$$p_{00} = 1 - (P_1 + p_{11}) = 1 - \frac{N_{AB} + N_{AB'} - N_{ABB'}}{N_A}. \tag{15}$$

We use the probability P_1 to scale our measured density matrix in the one-photon subspace $\hat{\rho}^{(1)}$ [Eq. (8)], yielding the matrix elements $p_{01} = P_1\beta$, $p_{10} = P_1\alpha$, and $d = P_1\gamma$. Since we determine the full complex γ in the single-photon subspace, we obtain the complex value of the off-diagonal matrix element d.

We can find a lower bound on the entanglement in our system by measuring the concurrence C of $\hat{\rho}^{(2)}$ [9,18]. The concurrence is given by

$$C = \max(2|d| - 2\sqrt{p_{00}p_{11}}, 0). \tag{16}$$

D. Measuring $g^{(2)}(0)$

A common figure of merit that describes the quality of the production of single-photon states is the degree of second-order coherence $g^{(2)}(0)$. Classical fields must satisfy the inequality $g^{(2)}(0) \geqslant 1$, while the degree of second-order coherence for a source containing exactly n photons is [21]

$$g^{(2)}(0) = 1 - \frac{1}{n}, \tag{17}$$

which is valid for $n \geqslant 1$. This means that an ideal source containing a single photon has $g^{(2)}(0) = 0$, while a source containing exactly two photons has $g^{(2)}(0) = 1/2$.

As was shown by Grangier *et al.*, the degree of second-order coherence of the signal beam, conditioned on the detection of an idler photon, can be expressed in terms of the measured photocounts as [19,20]

$$g^{(2)}(0) = \frac{N_A N_{ABB'}}{N_{AB} N_{AB'}}. \tag{18}$$

In our experiments we use the ten measurements with the phase settings $\phi_1 = \phi_2 = 0$ to determine $g^{(2)}(0)$.

III. EXPERIMENTS

In our experiments we use a 150 mW, 405 nm laser diode to pump a 3-mm-long β barium borate (BBO) crystal. This produces type-I spontaneous parametric down-conversion at 810 nm, with signal and idler beams making angles of 3° from the pump. The idler beam is focused into a single-mode, polarization-preserving optical fiber, filtered by RG780 colored glass and a 10 nm bandpass filter centered at 810 nm, and detected by a single-photon-counting module (SPCM), which we refer to as detector A. Detection of an idler photon heralds the production of a single photon in the signal beam. The signal beam is also focused into a single-mode, polarization-preserving optical fiber. The output of this fiber is then collimated and passed on to our interferometer.

Figure 1 represents a simplified version of our interferometer, while the interferometer that we actually use is shown in Fig. 2. This interferometer consists of two modified Sagnac interferometers in series; they are modified in the sense that the two counterpropagating directions do not overlap, but are spatially separated. Heralded single photons from the output of the signal-beam fiber strike the 50:50 beam splitter. Both the clockwise and counterclockwise beams pass through microscope slides, one of which is mounted to a tilt stage controlled by a stepper motor that allows us to adjust the phase ϕ_1 in a controlled manner. The fixed microscope slide in the other path is necessary to equalize both the path lengths and the dispersions of the two counterpropagating directions, a necessity for seeing high-visibility interference with our broad-bandwidth single-photon source. The counterpropagating beams of this first Sagnac interferometer recombine at the beam splitter, and the outputs become the counterpropagating beams of the second interferometer. The second interferometer also contains two microscope slides, one of which allows us to control ϕ_2 with a second stepper motor. The beams in the second interferometer recombine at the beam splitter before exiting.

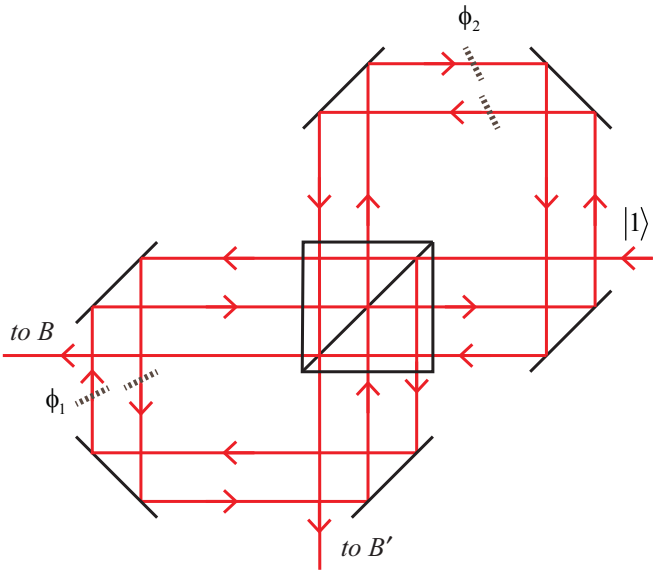

FIG. 2. (Color online) The series interferometers used in the experiments. Each modified Sagnac interferometer has microscope slides in each of the two counterpropagating beams. One of the slides in each interferometer is tilted under the control of a stepper motor in order to adjust the interferometer phase.

The interferometer outputs are coupled into multimode optical fibers, filtered with RG780 colored glass, and then detected with SPCMs. These detectors are referred to as B and B'. Counting of singles, twofold coincidences and threefold coincidences is performed using a coincidence counting unit implemented on an Altera DE2 board. The coincidence windows of the AB and AB' coincidences were measured to be 7.8 and 7.7 ns, respectively. We do not subtract accidental coincidences from our data, nor do we make any other corrections for detection efficiency, etc.

The single-photon entangled state $|\psi\rangle$ is created after the first beam-splitter reflection. The phase angle θ in the state is adjusted by adding an offset to the phase ϕ_1 (adding an offset of $-\theta$ to ϕ_1 creates a state with a phase of θ). We have chosen to use Sagnac interferometers, rather than Mach-Zehnder interferometers, for two reasons. The first is that high-visibility interference with our 10 nm bandwidth source requires that the pathlengths and dispersions of the beams be nearly perfectly matched; this is more easily achieved using Sagnac interferometers than Mach-Zehnder interferometers. Furthermore, because the counter-propagating beams in a modified Sagnac are nearly common-path, we find that these interferometers are extremely stable against phase drifts. This allows us to reliably adjust the phase angles ϕ_1 and ϕ_2 when performing our measurements, without needing to resort to active phase stabilization.

A. Phase calibration

In order to calibrate the phase of the first interferometer, ϕ_1, we block one of the beams in the second interferometer

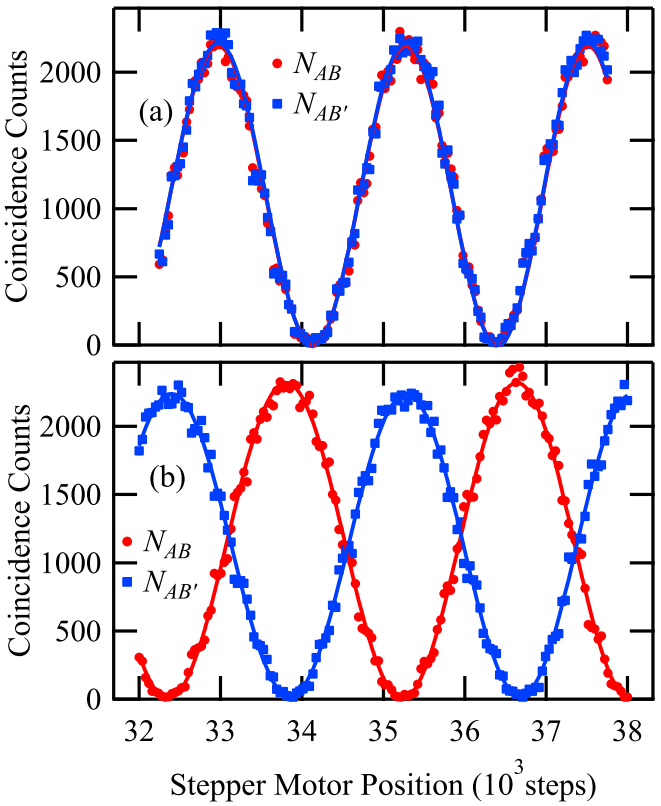

FIG. 3. (Color online) Coincidence counts in 3 s as a function of the position of the stepper motor that adjusts the interferometer phase. Results for scanning the phase of the first interferometer, ϕ_1, are shown in (a), while results for scanning the phase of the second interferometer, ϕ_2, are shown in (b). The measured data are shown as points, while fits to the measured data are shown as solid lines [the lines in (a) are essentially on top of each other].

and scan the stepper motor that tilts the microscope slide that adjusts this phase. Coincidence counts between the heralding detector A and detectors B and B' at the outputs of the interferometer are shown in Fig. 3(a). Notice that the interference patterns on each detector oscillate with the same phase. This is because by blocking one of the arms in the second interferometer we are monitoring a single output from the first interferometer. This single output splits equally on the final beam splitter, so we expect the two outputs to be the same. We fit these data with cosine functions, and from the fits we determine ϕ_1 as a function of the motor position. We find that ϕ_1 varies quadratically with the motor position. (The phase variation is predominantly linear, but there is a small quadratic contribution.) This calibration of ϕ_1 as a function of the motor position is used to set the phase in subsequent measurements used to perform tomographic state reconstruction.

In order to calibrate the phase of the second interferometer, ϕ_2, we follow the same basic procedure: We block one of the arms of the first interferometer and scan the stepper motor that tilts the microscope slide that adjusts ϕ_2. Coincidence counts that result from doing this are shown in Fig. 3(b). In this case we are blocking one of the inputs to the interferometer and monitoring the two outputs, so the fringe patterns are expected to be out of phase with each other, which is what we observe. Fits to this data show that ϕ_2 also varies quadratically with the motor position. The visibility of each of the interference patterns shown in Fig. 3, determined from the fits, is 98% or greater.

B. State measurements in the single-photon subspace

As described above, we perform ten total measurements and determine three different density matrices $\hat{\rho}^{(1)}$ in the subspace of a single photon. Each measurement has an integration time of 30 s.

We characterize our measured states using several quantities. The purity of the state is given by $P = \mathrm{Tr}[(\hat{\rho}^{(1)})^2]$, where Tr indicates the trace. Pure states have $P = 1$, while for any nonpure state $P < 1$. The amount of overlap between two states described by density matrices $\hat{\rho}_1$ and $\hat{\rho}_2$ can be expressed as the fidelity, F, which is defined as [14,23]

$$F = (\mathrm{Tr}[\sqrt{\sqrt{\hat{\rho}_1}\hat{\rho}_2\sqrt{\hat{\rho}_1}}])^2. \tag{19}$$

The fidelity takes on values $0 \leqslant F \leqslant 1$, with $F = 1$ corresponding to $\hat{\rho}_1 = \hat{\rho}_2$. We use F to quantify the overlap between the measured state and the state that we were attempting to prepare. When computing P and F, we use the density matrix obtained from all ten measurements; we referred to this as the standard model above.

Examples of measured density matrices, for states prepared in $|\psi_2\rangle$ and $|\psi_3\rangle$ [Eqs. (4) and (5)], are shown in Fig. 4. The purities and fidelities of these and other measured states are given in Table I; note that in all cases the states have $P \geqslant 0.95$ and $F \geqslant 0.97$. This means that we are able to prepare and measure the intended states with reasonably high purity and fidelity.

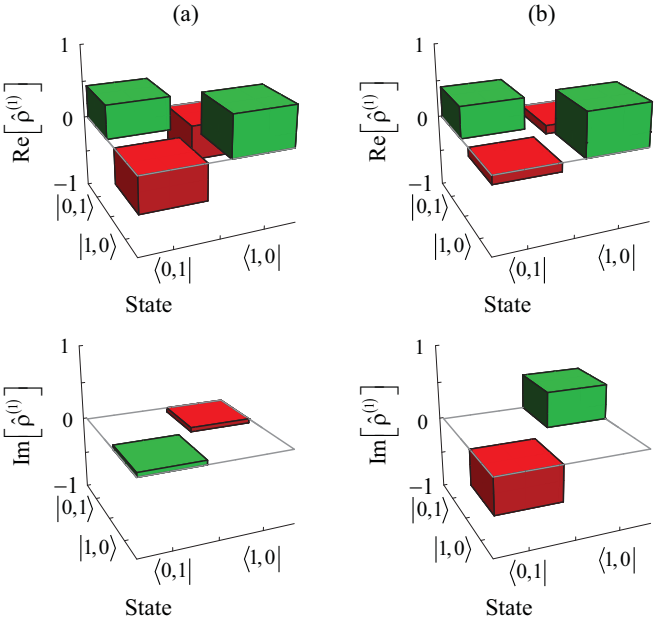

FIG. 4. (Color online) The real and imaginary parts of the measured density matrices $\hat{\rho}^{(1)}$, for measurements performed on states prepared in (a) $|\psi_2\rangle$ and (b) $|\psi_3\rangle$. Green boxes correspond to positive values, while red boxes correspond to negative values.

TABLE I. The columns in this table correspond to the following quantities: $|\psi\rangle$ is the state that is prepared, P is the purity of the measured state, F is the fidelity of the measured state when compared to $|\psi\rangle$, and $\Delta\Omega$ is the AIC difference.

$\|\psi\rangle$	P	F	$\Delta\Omega$
$\frac{1}{\sqrt{2}}(\|1,0\rangle + \|0,1\rangle)$	0.95	0.97	−5.7
$\frac{1}{\sqrt{2}}(\|1,0\rangle - \|0,1\rangle)$	0.97	0.98	−0.5
$\frac{1}{\sqrt{2}}(\|1,0\rangle + i\|0,1\rangle)$	0.99	0.97	−3.3
$\frac{1}{\sqrt{2}}(\|1,0\rangle - i\|0,1\rangle)$	0.98	0.97	−1.1

Also shown in Table I is the value of the AIC difference $\Delta\Omega$ for each of the measured states. The values in this table are for individual state measurements, but we find that they are typical values obtained when our system is well aligned and allowed to come to equilibrium. For example, we most often obtain values for $\Delta\Omega$ between −10 and 0, but we do measure lower values. Since the measured values of $\Delta\Omega$ are negative, there is some drift in our states and thus the alternative model using two density matrices is a better description for our states than a single density matrix [15]. However, the question that remains is just how much change is represented by these values of $\Delta\Omega$. One reason to suspect that the states do not change very much is that for each model the values of the AIC in our experiments are on the order of −200 000, so the values of $\Delta\Omega$ in Table I represent a difference of less than a few parts in 10^5.

Another way to quantify the state drift is to examine the differences between the two density matrices that constitute the alternative model (these density matrices are measured one right after the other). For the state depicted in Fig. 4(a), we find that the difference in the parameter β [Eq. (8)] for these two density matrices is $\Delta\beta = 0.005$, and the difference in the phase of the complex parameter γ is $\Delta\theta = 0.008$ rad. We also find that if we compute the fidelity of these two matrices, we obtain $F = 0.9999$, so they are very close to each other in Hilbert space.

We have also performed Monte Carlo simulations of our data, using the same average counting rates, etc., that we have in our experiments. We simulate 1000 experimental runs and look at the statistics of $\Delta\Omega$ and other parameters. If we include the effects of Poissonian fluctuations of the photocounts and accidental coincidences, but no phase drift or fluctuations in our interferometer, we find that $\Delta\Omega = 1.5 \pm 1.3$ (here, and for all of the data from the simulations, the error bars are one standard deviation), and 89% of the simulated trials yield positive values for $\Delta\Omega$. If we add phase fluctuations having a mean of 0 and a standard deviation of $\pi/400$(0.008 rad) to ϕ_1 and ϕ_2, we find $\Delta\Omega = -4.3 \pm 5.1$, and only about 18% of the trials yield positive values of $\Delta\Omega$. For these parameters the simulations yield $\Delta\beta = 0 \pm 0.003$ and $\Delta\theta = 0 \pm 0.005$ rad. If we simulate a phase shift of the state between state measurements ($\Delta\theta$) of $\pi/400$ and maintain the standard deviation of the phase fluctuations at $\pi/400$, the results are essentially the same, except that $\Delta\theta = 0.008 \pm 0.005$ rad.

The results of the simulations with phase drift and fluctuations on the order of $\pi/400$ are consistent with our experimental measurements. We conclude from this that the predominant source of state drift in our experiments is drift and fluctuations of approximately this size in the phases of our interferometer. So, while our measurements are sensitive to changes in the state over the 5 min that it takes us to measure it, the state actually changes very little.

C. Entanglement in the larger Hilbert space

As described in Secs. II C and II D, immediately after performing the measurements that determine $\hat{\rho}^{(1)}$, we perform ten more measurements with $\phi_1 = \phi_2 = 0$ in order to determine $\hat{\rho}^{(2)}$ [Eq. (12)], C [Eq. (16)], and $g^{(2)}(0)$ [Eq. (18)]. We use 60 s integration times for each of these measurements. We integrate longer than we do when determining $\hat{\rho}^{(1)}$ because here we need to determine the probability of having one photon in each arm of the interferometer, p_{11}, which is a low-probability event. Getting good statistics on this quantity requires a longer integration time.

The magnitude of $\hat{\rho}^{(2)}$, corresponding to the same state as that depicted in Fig. 4(a), is shown in Fig. 5. Table II shows the measured values of several other quantities, all corresponding to the same states that are listed in Table I. Here we see that the largest density matrix element corresponds to having no photons in the interferometer. Our heralding efficiency is approximately 9%, leaving no photons in our interferometer about 91% of the time. The probability of having one photon in each arm of the interferometer is on the order of 10^{-5}, which yields values for $g^{(2)}(0)$ that are approximately 0.01. These values are consistent with those arising from the expected accidental coincidence rates in our system, and indicate that our states contain only a very small two-photon contribution [24].

Finally, in Table II we see that our values for the concurrence are $C \cong 0.08$. The concurrences are larger than 0 by between 45 and 89 standard deviations, so we can say with confidence that our states are entangled. The concurrence is currently limited by the ∼9% overall heralding efficiency of our source.

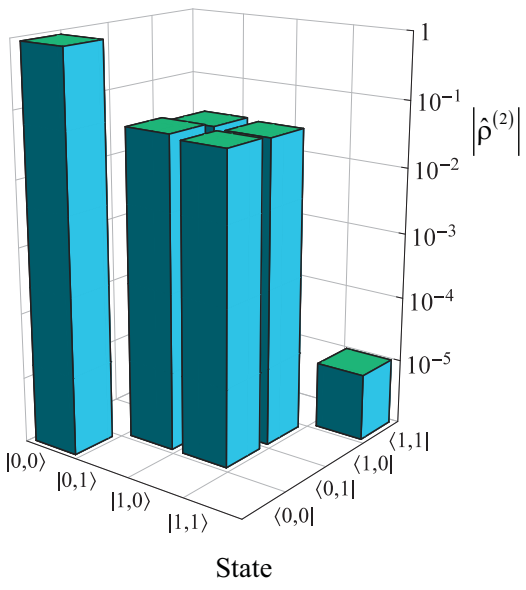

FIG. 5. (Color online) The magnitude of the density matrix $\hat{\rho}^{(2)}$, corresponding to the same state as depicted in Fig. 4(a). While our measurements determine the full complex $\hat{\rho}^{(2)}$, we plot only the magnitude in order to use a logarithmic scale on the vertical axis.

TABLE II. The columns in this table correspond to the following quantities: C is the concurrence, $g^{(2)}(0)$ is the degree of second-order coherence, p_{00} is the probability of detecting zero photons, p_{11} is the probability of detecting one photon in each beam. The errors represent one standard deviation.

$\|\psi\rangle$	C	$g^{(2)}(0)$	p_{00}	p_{11}
$\frac{1}{\sqrt{2}}(\|1,0\rangle + \|0,1\rangle)$	0.0796 ± 0.0014	0.010 ± 0.003	0.9060 ± 0.0004	$2.2 \times 10^{-5} \pm 0.7 \times 10^{-5}$
$\frac{1}{\sqrt{2}}(\|1,0\rangle - \|0,1\rangle)$	0.0857 ± 0.0019	0.005 ± 0.003	0.9043 ± 0.0004	$1.0 \times 10^{-5} \pm 0.7 \times 10^{-5}$
$\frac{1}{\sqrt{2}}(\|1,0\rangle + i\|0,1\rangle)$	0.0805 ± 0.0009	0.013 ± 0.002	0.9076 ± 0.0002	$2.8 \times 10^{-5} \pm 0.5 \times 10^{-5}$
$\frac{1}{\sqrt{2}}(\|1,0\rangle - i\|0,1\rangle)$	0.0826 ± 0.0010	0.011 ± 0.002	0.9054 ± 0.0003	$2.6 \times 10^{-5} \pm 0.5 \times 10^{-5}$

Our detectors have a detection efficiency of 60%, and we find that the coupling efficiency of our source into the single-mode fibers yields a heralding efficiency of ∼20%. Losses in the interferometer and coupling into the detector fibers then reduce the heralding efficiency to ∼9%.

IV. CONCLUSIONS

We have prepared single-photon entangled states (states of a single photon that takes two paths) and then characterized these states in several ways. In the subspace of a single measured photon, we determine the density matrices of these states with maximum-likelihood quantum-state tomography. We are able to prepare these states with high fidelity ($F \geqslant 0.97$), and the measured states are found to be reasonably pure ($P \geqslant 0.95$). We have used the Akaike information criterion and Monte Carlo simulations to help us estimate the amount of time-dependent drift in our states. We find that the state drift is influenced by phase drifts and fluctuations on the order of $\pi/400$ in our apparatus.

We also perform measurements in the larger space consisting of up to one photon in each mode, and determine density matrices in this space. We find that the concurrences of these density matrices are $C \cong 0.08$, and are positive by at least 45 standard deviations for all of our measured states, indicating that our states are indeed entangled. Simultaneous measurements of $g^{(2)}(0)$ confirm that the two-photon component to our states is quite small.

Note that our interferometer is largely independent of the polarization of the photons [25]. As such we will be able to use our apparatus and measurement technique to perform state measurements on single photons that are entangled not only in the path that they take, but in polarization as well.

ACKNOWLEDGMENTS

We thank S. J. van Enk for several very valuable discussions. This work was supported in part by the Whitman College Louis B. Perry Summer Research Endowment and the Parents Student-Faculty Research fund.

[1] S. M. Tan, D. F. Walls, and M. J. Collett, Nonlocality of a Single Photon, Phys. Rev. Lett. **66**, 252 (1991).
[2] S. J. van Enk, Single-particle entanglement, Phys. Rev. A **72**, 064306 (2005).
[3] N. Sangouard, C. Simon, H. de Riedmatten, and N. Gisin, Quantum Repeaters Based on Atomic Ensembles and Linear Optics, Rev. Mod. Phys. **83**, 33 (2011).
[4] S. A. Babichev, J. Appel, and A. I. Lvovsky, Homodyne Tomography Characterization and Nonlocality of a Dual-Mode Optical Qubit, Phys. Rev. Lett. **92**, 193601 (2004).
[5] O. Morin, J.-D. Bancal, M. Ho, P. Sekatski, V. D'Auria, N. Gisin, J. Laurat, and N. Sangouard, Witnessing Trustworthy Single-Photon Entanglement with Local Homodyne Measurements, Phys. Rev. Lett. **110**, 130401 (2013).
[6] F. Monteiro, V. C. Vivoli, T. Guerreiro, A. Martin, J. D. Bancal, H. Zbinden, R. T. Thew, and N. Sangouard, Revealing Genuine Optical-Path Entanglement, Phys. Rev. Lett. **114**, 170504 (2015).
[7] B. Hessmo, P. Usachev, H. Heydari, and G. Björk, Experimental Demonstration of Single Photon Nonlocality, Phys. Rev. Lett. **92**, 180401 (2004).
[8] M. Fuwa, S. Takeda, M. Zwierz, H. M. Wiseman, and A. Furusawa, Experimental proof of nonlocal wavefunction collapse for a single particle using homodyne measurements, Nat. Commun. **6**, 6665 (2015).
[9] C. W. Chou, H. de Riedmatten, D. Felinto, S. V. Polyakov, S. J. van Enk, and H. J. Kimble, Measurement-induced entanglement for excitation stored in remote atomic ensembles, Nature (London) **438**, 828 (2005).
[10] K. S. Choi, H. Deng, J. Laurat, and H. J. Kimble, Mapping photonic entanglement into and out of a quantum memory, Nature (London) **452**, 67 (2008).
[11] K. C. Lee *et al.*, Entangling macroscopic diamonds at room temperature, Science **334**, 1253 (2011).
[12] I. Usmani, C. Clausen, F. Bussieres, N. Sangouard, M. Afzelius, and N. Gisin, Heralded quantum entanglement between two crystals, Nat. Photon. **6**, 234 (2012).
[13] D. Salart *et al.*, Purification of Single-Photon Entanglement, Phys. Rev. Lett. **104**, 180504 (2010).
[14] J. B. Altepeter, E. R. Jeffrey, and P. G. Kwiat, Photonic state tomography, in *Advances in Atomic, Molecular and Optical Physics*, edited by P. R. Berman and C. C. Lin (Elsevier, Amsterdam, 2006), p. 105.
[15] S. J. van Enk and R. Blume-Kohout, When quantum tomography goes wrong: Drift of quantum sources and other errors, New J. Phys. **15**, 025024 (2013).
[16] K. Usami, Y. Nambu, Y. Tsuda, K. Matsumoto, and K. Nakamura, Accuracy of quantum-state estimation utilizing Akaike's information criterion, Phys. Rev. A **68**, 022314 (2003).

[17] G. Mădălin, K. Theodore, and D. Ian, Rank-based model selection for multiple ions quantum tomography, New J. Phys. **14**, 105002 (2012).
[18] W. K. Wootters, Entanglement of Formation of an Arbitrary State of Two Qubits, Phys. Rev. Lett. **80**, 2245 (1998).
[19] P. Grangier, G. Roger, and A. Aspect, Experimental evidence for a photon anticorrelation effect on a beam splitter: A new light on single-photon interferences, Europhys. Lett. **1**, 173 (1986).
[20] Grangier *et al.*, [19] referred to this parameter as α.
[21] R. Loudon, *The Quantum Theory of Light* (Oxford University Press, Oxford, 2000).
[22] J. J. Thorn, M. S. Neal, V. W. Donato, G. S. Bergreen, R. E. Davies, and M. Beck, Observing the quantum behavior of light in an undergraduate laboratory, Am. J. Phys. **72**, 1210 (2004).
[23] S. M. Barnett, *Quantum Information* (Oxford University Press, Oxford, 2009).
[24] M. Beck, Comparing measurements of $g^{(2)}(0)$ performed with different coincidence detection techniques, J. Opt. Soc. Am. B **24**, 2972 (2007).
[25] The most significant difference between the two polarizations is in the reflectivity of the beam splitter. For our beam splitter (Newport 20BC17MB.2) this difference is approximately 4%.